Laboratory Report

MECH 656

Fundamentals of Turbulent Flows

Gaétan RAYNAUD

2022063 - gaetan.raynaud@polymtl.ca

260964987 - gaetan.raynaud@mail.mcgill.ca

23 avril 2020

Table des matières

1   Introduction

From an engineering point of view, turbulence is most of the time problematic. Growth of turbulence turns usually to be an excitation for others phenomena, instabilities at a larger scale that can seriously damage the entire structure and put lives in danger. In terms of wall-bounded turbulence and more specifically channel flows, many examples are to be found in transport and energy sectors.

One of the most thrilling engineering project lie in space race : a giant step has been taken dealing with the huge task of building a spacecraft carrying people with very few computing capabilities compared to today's ones. One of these challenges is to assure the stability of the rocket engine that propel reacting fluids at a tremendous Reynolds number that may induce pressure oscillations and then structural vibrations [Strahle and Neale, 1981]. Turbulent-induced vibrations is indeed a worrying problem that faced nuclear engineering too [Weaver et al., 2000].

These problematic have justified a big amount of research on channel flows to understand and verifies the theoretic predictions like we modestly do in this lab report, as well as fit some turbulent models. Today research is still conducted on turbulent wall-bounded flows but with some positive insights on turbulence : energy harvesting for instance [Goushcha et al., 2015].

2   Theoretical Background

This lab will address two major points in the theoretical predictions of turbulent flows : wall bounded shear layers and statistics of turbulence.

2.1   Wall bounded flow

Turbulent boundary layers reveals several characteristic length scales linked with different phenomena : from the geometrical length (channel's radius h), moving through the boundary layer thickness δ to the smallest scale where viscosity dominates, there is a continuous transition between ranges at which specific phenomena occur. A great amount of literature exists on this topic (see for instance [Tennekes et al., 1972] and [Pope and Pope, 2000]) and this introduction only aims at recalling the major results that will be discussed in the following sections.

We will limit ourselves to an incompressible flow in an aerodynamically smooth channel. The considered fluid, air here, is of kinematic viscosity ν and density ρ. From the conservation equations of turbulent quantities, we can derive the shear stress evolution through the y direction (radius direction) that is equal at the wall to

$$\tau(y = 0) = \tau_w = \rho\nu \left(\frac{d\bar{U}}{dy} \right)_{y=0} \tag{1}$$

This quantity is the relevant scale near the wall since turbulent quantities such as $\overline{uv} \to 0$. It

is used to define the typical velocity and length scale of viscosity effects :

$$u_* = \sqrt{\tau_w/\rho} \tag{2}$$
$$\delta_\nu = \nu/u_* \tag{3}$$
$$\tag{4}$$

Near the wall we will therefore deal with y^+ and u^+ that are the y-distance to the wall and the u turbulent velocity fluctuations made dimensionless by previous length scales :

$$y^+ = y/\delta_\nu \tag{5}$$
$$u^+ = u/u_* \tag{6}$$

In the intermediate region where $\delta_\nu << y << h$, we will use an other non-dimensionnalisation based on channel radius h and mean-flow velocity at centre line U_0 :

$$\eta = y/h \tag{7}$$

The main results are that :

1. In the viscous sublayer, up to $y^+ \lesssim 5$

$$u^+ = y^+ \tag{8}$$

2. In the inertial sublayer, where $y^+ >> 1$ and $\eta << 1$:

$$\frac{\bar{U} - U_0}{u_*} = \frac{1}{\kappa}\ln(\eta) + b \tag{9}$$

$$\frac{\bar{U}}{u_*} = \frac{1}{\kappa}\ln(y^+) + a \tag{10}$$

Where $a \approx 5.2$ and $\kappa \approx 0.41$ are universal whereas b is flow-dependent.

2.2 Statistics of turbulence

Turbulence is a random process and may therefore be looked at using adapted tools from the field of statistics. These can classified in three groups : indicators of data distribution, spectral analysis and correlations detection. These two lasts often work together.

We will consider random variables that are speeds values here, mainly $\tilde{u} = \bar{U} + u$ taking values in $\mathbb{R}$ with a probability function $P : \mathcal{P}(\mathbb{R}) \to [0,1]$. Here $\bar{}$ will denote averaging and we define the cumulative distribution function CDF and the Probability density function PDF as :

$$CDF_u : x \to P(u \leq x) \tag{11}$$

$$PDF_u : x \to \frac{d}{dx}CDF_u(x) \tag{12}$$

We will also deal with n^{th} order central moment of the distribution defined as $\overline{u^n}$ which will allow us to find u_{rms} ($n = 2$), Skewness ($n = 3$) or Kurtosis ($n = 4$) with appropriate dimensionnalisation.

Furthermore we will introduce spectral analysis with time and spatial Fourier transform. We will then be able to extract the contribution of a phenomena, for instance kinetic energy of turbulence (TKE), from different scales, frequencies f or wave numbers κ. For spatial transformation, one of the major prediction is to be found with Kolmogorov similarity hypothesis that state that these spectrum quantities at high Reynolds number only depend of fluid viscosity ν and dissipation rate of TKE ε and are universal. And in the inertial sublayer, as viscosity effects are neglictable, these spectra should only depend on ε (and κ). As no dimensionless quantity can be made out of ε and κ, there must be a power law relation that can be determined with dimensional analysis.

3 Experimental equipment and procedure

3.1 Context and measurement procedure

As we expect a logarithmic evolution in the inertial sublayer, distance from the wall y of the measurement points might be chosen wisely. Indeed there are few variations in the central region so it could be a waste of data to outnumber measurements there. The minimal distance is given by the hot-wire that cannot be infinitely close to the wall for practical reasons (its width and safety reasons). This $y_{min} = 0.13$ mm gives a bound for an equal logarithmic distribution of 15 measurements as presented at figure 1 that we would have chosen. Comparison is proposed with given points. We can remark that a compromise have been made for small scale behaviour (where a linear relation is to be found).
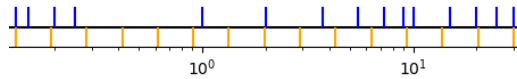

FIGURE 1 – Position of 15 hot wire measurement points on y axis (log scale, millimetres). Given ones (blue superior lines) and equally distributed (lower orange lines) between $y_{min} = 0.13$ mm and $h = 30$ mm

At these 15 points will be sampled time series data for PDF determination. Besides at 3 of these points are provided larger data measurements (at higher sampling frequencies) so that a spectrum can be computed with a sufficient resolution.

During the experiment, the channel fan is set to blow air at an approximate centre line velocity of $U_0 \sim 5$ m/s which correspond to a Reynolds number of $Re = U_0 D/\nu \sim 2 \times 10^5$. This is far above the threshold for a fully developed turbulence in a channel flow empirically located around $Re \sim 2900$.

4

3.2 Anemometer calibration

Measurements of speed are obtained with hot-wire anemometry technique. It consists of a very thin wire that is immersed in a fluid flow. An electric current goes through the wire and heat it up (Joule's effect). The temperature reached depends on the thermal dissipation by the flow (with a conductive and convective part) so that at a given current, each flow speed leads to a determined wire temperature. The narrowness of the wire might let us assume that the wire temperature reaches its equilibrium at a given flow speed before speed flow actually changes (so that we don't have to deal with time variation of temperature in the wire). This should nonetheless give a frequency threshold for time scale of speed variations that are shorter than the time scale of wire temperature variation.

As a classical ohmic resistor, resistance of the wire changes with its temperature. Measuring resistance variation from its usual value provide a way of computing speed changes. For instance Wheatstone bridge is a common electrical circuit for obtaining the resistance value through a tension measurement. Nonetheless, this relation between flow speed and voltage has to be determined empirically since it depends of the room temperature, usual resistance, geometry and materials properties of the wire...
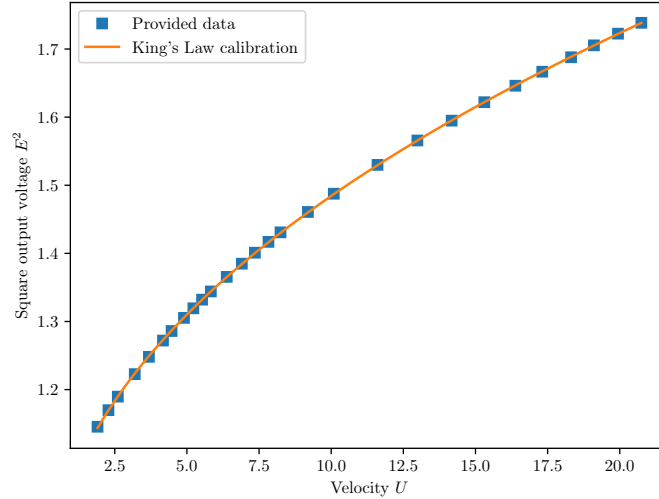

FIGURE 2 – Calibration of King's Law coefficients $A = 8.44 \times 10^{-1}$ V^2, $B = 2.23 \times 10^{-1}$ uSI and $n = 0.458$ with a L2-normalized residual rms $e_{rms} = 4.6 \times 10^{-4}$

Calibration's results are presented on figure 2 and obtained with `Python`'s file `CalibrationAnemometer.py`. It consists of a minimization process in $\mathbb{R}^3$ of parameters A, B and n. For a set of data $y \in \mathbb{R}^p$, we minimize the following quantity :

$$\min_{(A,B,n)\in\mathbb{R}^3} \frac{\sqrt{\frac{1}{p}\sum_y \left(E^2(y) - A - BU^n(y)\right)^2}}{\sqrt{\frac{1}{p}\sum \left(E^2\right)^2}} \tag{13}$$

4 Results

In figure 3 we represent the mean velocity profile in a log-lin scale with a fitting of the log-law performed on the central points. More precisely, the excluded points are the two first (sorted by y) since they visually are out of the region where most of the points seems aligned. Moreover I chose not to take into account the four last points for the log-law fitting because their are located quite far beyond the empirical threshold $\eta = 0.3$.

At this point there is no numerical value for the threshold $y^+ = 30$ yet because we need u_* to compute y^+. And one way of determining u_* is using the log-law fitting. u_* could also have been determined using the linear law in the very near region to the wall where $u^+ = y^+$ with a linear fitting of slope α and $u_* = \sqrt{\nu\alpha}$ but the imprecision is too high at this stage. Indeed the method using the log-law fitting gives $u_* = 2.30 \times 10^{-1}$m/s while a fitting with the two first points of the linear law gives $u_* = 1.53 \times 10^{-2}$m/s.

The root-mean-square profile of average-free speed u_{RMS} is plotted at figure 4 and the skewness S_u is depicted at figure 5 with :

$$u_{RMS} = \sqrt{< \left(\tilde{u} - \bar{U} \right)^2 >} \tag{14}$$

$$S_u = \frac{< \left(\tilde{u} - \bar{U} \right)^3 >}{u_{RMS}^3} \tag{15}$$

The probability density function (PDF) for the three locations is presented at figure 6.b. It is obtained by a custom written function which is avalaible in the github repository. The PDF is obtained from the reconstruction of the CDF which is quite easy, following the method explained in algorithm 1. It can be noted that steps 4 and 5 could be done in the inverse order. The filtering at step 5 uses the scientific `Python` library `scipy` with the zero-phase filtering function `filtfilt` configured with a 3$^{\text{rd}}$-order butterworth low-pass filter with hand-tuned frequency cut.

As depicted on Fig. 7.a, the obtaining of E is not trivial. Theoretically, according to [Pope and Pope, 2000] (eq. 6.217) and [Tennekes et al., 1972] (eq. 8.1.13) one should obtain E from one-dimensional spectrum F_{11} in isotropic case with the relation :

$$E(\kappa) = \kappa^3 \frac{d}{d\kappa} \left[\frac{1}{\kappa} \frac{dF_{11}(\kappa)}{d\kappa} \right] \tag{16}$$

But derivation with respect to κ amplifies the noise in the spectrum which is distorted by the $1/\kappa$ factor while derivating the second time. A filtering process is therefore required. The first is proceed on $F_{11}(\kappa)$ on a linear scale both for x-axis κ and y-axis F_{11}. A 5$^{\text{th}}$-order low pass numerical butterworth filter is used with a hand-tuned frequency cut. Then derivation is proceeded two times with a first order schema $dy/dx \approx (y(x_{k+1}) - y(x_k))/(x_{k+1} - x_k)$. E is finally filtered too with a similar filter but with changes in low-pass frequency.

Algorithm 1: PDF calculation

Result: Return vectors u_{PDF} and PDF_u

Step 1 : get time series data u;

Sort in ascending order $u \rightarrow u_{sorted}$;

Step 2 : Computing the CDF;

for $k = 0$ *to length of* u_{sorted} **do**

    delete duplications of u_{sorted}'s values ;

    if $u_{sorted}[k] > u_{sorted}[k-1]$ **then**

        $u_{sorted}[k]$ is appended to u_{PDF};

        Relative position in sorted data $k/\text{length}(u_{sorted})$ is appended to CDF_u;

    end

end

Step 3 : Interpolation of CDF on a regular range of u_{CDF} to ease derivation and filtering;

Step 4 : Derivation of CDF with respect to $u_{CDF} \rightarrow PDF_u^{noisy}$;

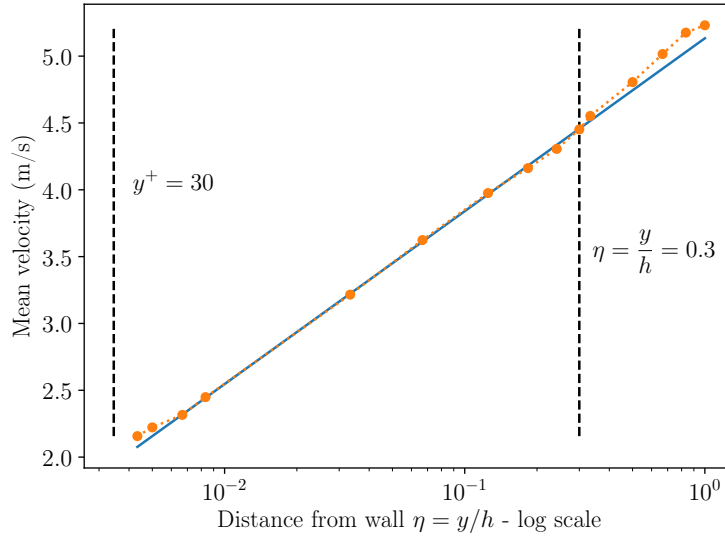**Step 5** : Denoising of PDF with a low-pass filter;

FIGURE 3 – Mean velocity profile displayed in a log-lin scale (dashed lines and orange points). Fitting with a log-law with a normalized RMS error of 4.77×10^{-3}
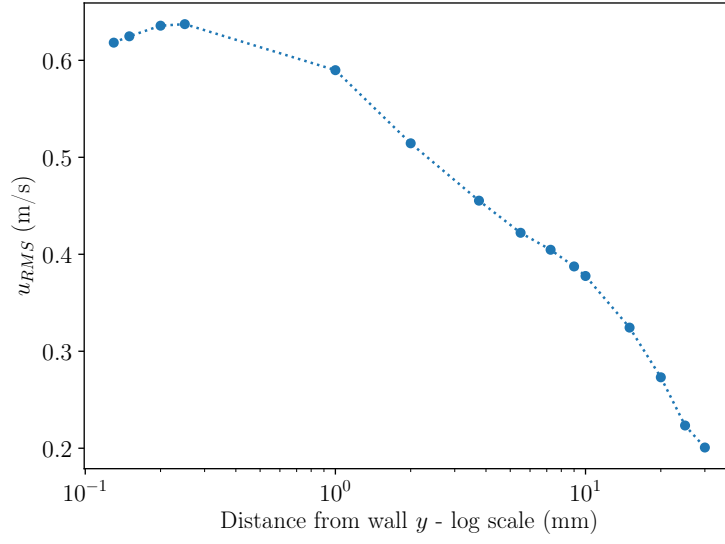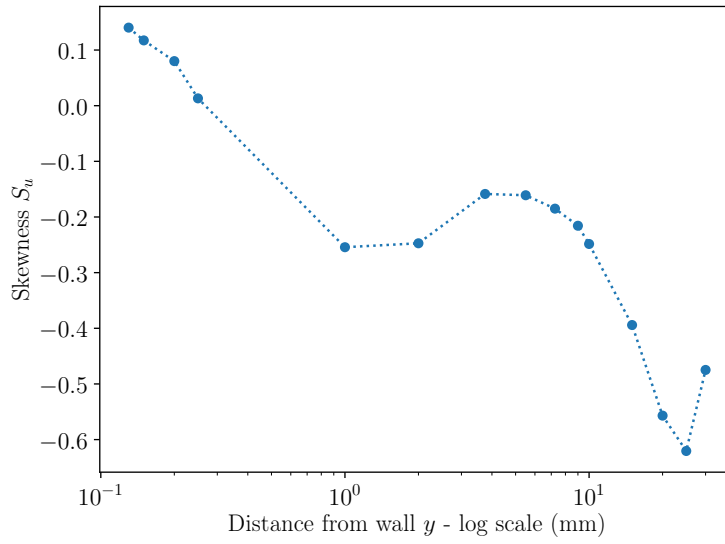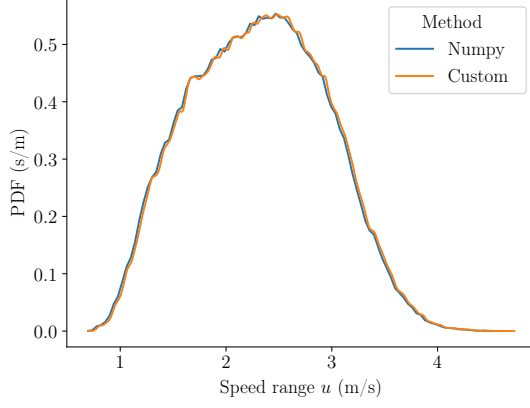
FIGURE 4 – RMS Profile plotted in log-lin scale

FIGURE 5 – Skewness profile S_u displayed in log-lin scale
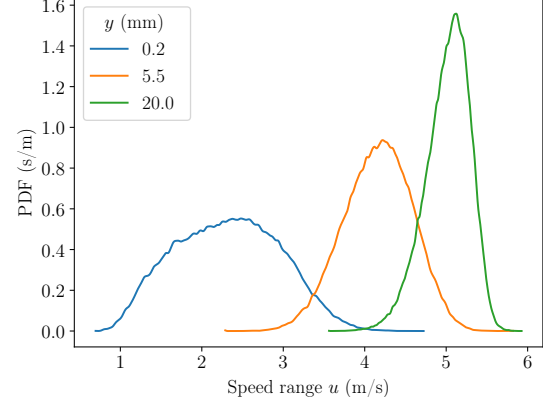
FIGURE 6 – a. Comparison of custom written PDF function with filtering frequency $f_{LP}^{PDF}/f_s = 5 \times 10^{-2}$ and PDF obtained from histogram function from Numpy library b. PDF displayed for the 3 locations.
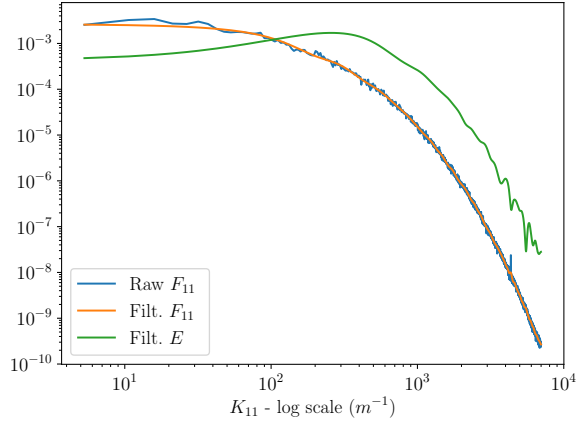
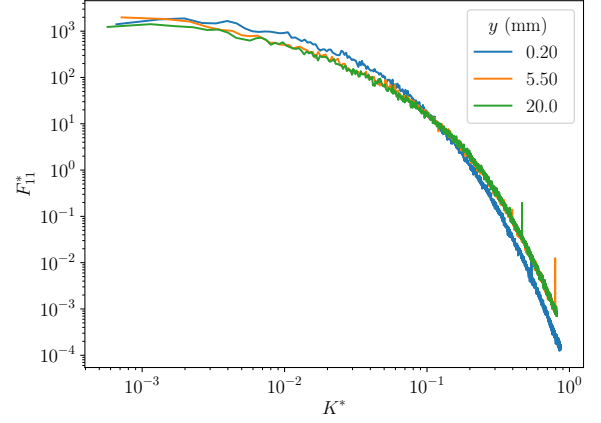FIGURE 7 – a. Illustration of the main stages of filtering and derivating E from F_{11}. b. Comparison of the one-dimensional spectra F_{11} at three locations y in a dimensionless form (see [Tennekes et al., 1972])
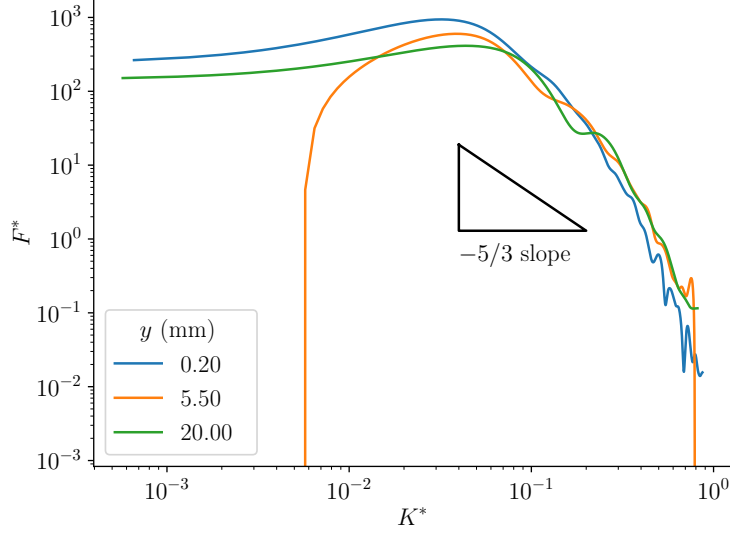
FIGURE 8 – Comparison of isotropic spectra E at three positions y with Kolmogorov $-5/3$ power spectrum law

5 Discussion

5.1 Mean velocity log-law agreement

From a qualitative point of you, the agreement with the log-law in the inertial sublayer is very good and validated by the normalized error at a low level :

$$\varepsilon_{RMS} = \sqrt{\frac{< \left(\bar{U} - u_{\text{log-law}} \right)^2 >}{< \bar{U}^2}} > = 4.77 \times 10^{-3} \tag{17}$$

with

$$u_{\text{log-law}} = A \ln y + B \tag{18}$$

where y is the dimensional distance from the wall (expressed in m). To determine the quantitative agreement with the universal constants of the log-law, we need to determine u_* since we have

$$\frac{\bar{U}}{u_*} = \frac{1}{\kappa} \ln(\frac{yu_*}{\nu}) + a \tag{19}$$

with the notation from [Tennekes et al., 1972] (eq. 5.2.27). One way of determining it is considering a and κ as given and using them to determine u_* and kinematic viscosity ν and compare it to standards values for air. This is achieved with the following relations :

$$u_* = A \times \kappa \tag{20}$$

$$\nu = u_* \exp \left[-\kappa \left(\frac{B}{u_*} - a \right) \right] \tag{21}$$

Numerical values are summarized in table 1. It is complicated to compare the friction velocity u_* with our available data but it seems to be in the same order of magnitude that u_{RMS}

10

in the central region. Besides, the kinematic viscosity of air derived from the log-law fitting is slightly lower than expected : around 1.5×10^{-5} m²/s at 1 atm. It is though in the right order of magnitude.

<div align="center">

TABLE 1 – Numerical values for the log-law fitting

	A	B	κ	a	u_*	ν
Numerical value	5.62×10^{-1}	7.10	0.41	5.2	2.30×10^{-1}	6.27×10^{-6}
Unit	m/s	m/s	-	-	m/s	m²/s

</div>

What seems to be the transition to viscous sublayer (or with a buffer layer) at low y^+ is less satisfying from a qualitative point of view. If we compare it to figure 5.6 in [Tennekes et al., 1972] or Fig 7.20 in [Pope and Pope, 2000] where speed u^+ drops quickly (graphically concave in log-lin scale), in figure 3, the velocity profile seems to go rather convex at low distance from the wall. Moreover, when plotted on a linear scale, the straight line fitting with the 2 or 3 first points is far from being equal to 0 at $y^+ = 0$.

If we recall that u_* is defined as $u_* = \sqrt{\tau_w/\rho}$, determining the **wall shear stress** τ_w is equivalent to estimate u_*. This have been talked about previously but let's sum up three methods for getting it :

1. Fitting the linear law in the viscous sublayer, i.e. finding $\alpha \in \mathbb{R}$ such as $\bar{U} = \alpha y$ (m/s). Then as we know from equation 8 that $\bar{U}/u_* = y u_*/\nu$ one can obtain u_* from

$$u_* = \sqrt{\alpha \nu} \tag{22}$$

2. Fitting the log-law in the inertial sublayer in dimensional form, i.e. finding $(A, B) \in \mathbb{R}^2$ such as $\bar{U} = A \ln y + B$ (m/s). Then using equation 9 given in η, we have the equality of logarithmic slope :
$$u_* = A\kappa \tag{23}$$

3. Using the same fitting of the log-law in a dimensional form than previously, we can take advantage of the universality of $a \approx 5.2$. According to equation 10,

$$\bar{U} = u_* \left(\frac{1}{\kappa} \ln y + a + \frac{1}{\kappa} \ln(u_*/\nu) \right) = A \ln y + B$$

So we can solve the implicit equation in u_* on the constant part :

$$B = u_* \left(a + \frac{1}{\kappa} \ln \left(\frac{u_*}{\nu} \right) \right) \tag{24}$$

Previously we have chosen the second possibility because it seems to be the most adequate in our case : no need of knowing precisely the actual value of viscosity of the fluid (which varies significantly with temperature...). Moreover we did not have a sufficient number of points for a fitting in the viscous sublayer (option 1).

<div align="center">11</div>

5.2 Comments on Skewness and RMS speed profile

The RMS speed profile plotted at figure 4 displays a maximum around $y = 0.25$ mm. This result could be expected from the following qualitative reasoning : near the wall, the no-slip condition implies that $\tilde{u} = 0$ so $u_{RMS} = 0$ too. As $u_{RMS} > 0$ and turbulence does its work, u_{RMS} increases with y. But as it gets closer to the centre line, large scale gradients S_{ij} get smaller and so does the production of turbulence's kinetic energy which explain why u_{RMS} decreases when $\eta \to 1$.

Skewness profile depicts a more complicated behaviour at figure 5 but there is a few things to comment though. As Skewness is a measurement of the distorsion of speed values variation, a zero skewness value implies a symmetric PDF and it seems to occur at $y = 0.25$ mm, which appears to be the location of the maximum of u_{RMS}. The global shape of S_u is coherent with what can be found into literature as [Mathis et al., 2011] for instance. If we look at the three curves depicted at figure 6.b, blue solid line (representing the PDF at $y = 0.2$ mm) depicts a density function that has a loss of balance on the right : values on the right side of the average are located farther than those on left side and so S_u is positive. On the contrary, the green solid line (representing the PDF at $y = 20$ mm) lacks of balance on the left where S_u is negative.

5.3 Comments on density functions

According to figure 6.a where the custom PDF function is compared to normalized histogram function from `Numpy`'s library, our method and the chosen filtering seems to be valid. Moreover for the three PDF depicted at figure 6.b, the integral minus 1 is kept under $1/N_{reg}$ where N_{reg} is the length of the regular range of u values on which is interpolated the CDF. From a practical point of view, the gap of PDF integral to unit is negligible for $N_{reg} \gtrsim 10^3$ an consolidate the presented approach.

One way of normalize the PDF axis to plot all the curves is to apply an affine transform on u-axis so that the new data are mean free and of standard deviation equal to 1. This can be summarized as :

$$x \to \hat{x} = \frac{x - \overline{x}}{\sqrt{\overline{x^2}}} \tag{25}$$

$$PDF_x \to PDF_{\hat{x}} = \sqrt{\overline{x^2}} PDF_x \tag{26}$$

As demonstrated in the final exam, the PDF has to be multiplied by standard deviation (which is here equal to u_{rms}) so that $\int PDF_x(x)dx = \int PDF_{\hat{x}}(\hat{x})d\hat{x} = 1$. From PDF we can get the CDF back by a basic integration as it is shown at figure 9.

At table 2 we compare distribution values obtained directly from the analysis program and those computed using data at centreline. We can notice that for the average and the root-mean-square mean-free velocity, the relative error to the analysis program is negligible. Nonetheless there is a quite noticeable difference for the skewness. Although the sign and the order of magnitude is good, having 15 percent of difference while u_{rms} is below 0.1 % is a bit unexpected.
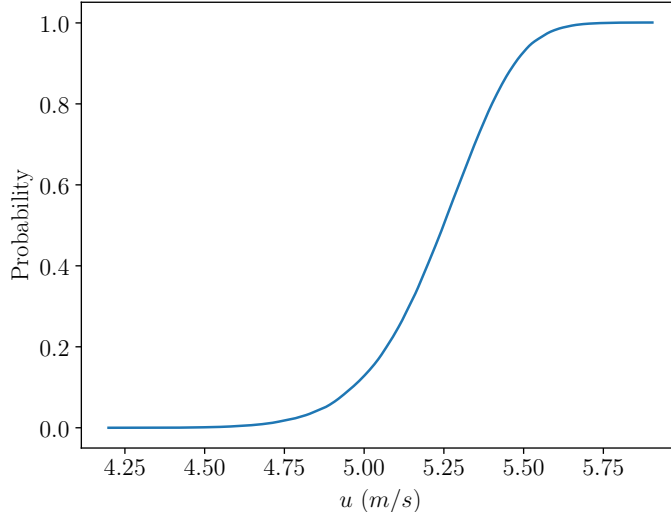
FIGURE 9 – Cumulative distribution function (CDF) computed from data at centreline ($y = 30$ mm)

We can try to explain this error by the fact that the extreme values taken by u are "cut" while computing the PDF since there are values of u that happen to be outside boundaries of the PDF x-axis that are mixed together with the boundary values. Moreover the 3rd power tends to increase the differences in comparison to the square root of u_{rms} that packed the distance. On the contrary, after having a look inside the `Fortran` code source, the programm seems to compute the third central moment on the move, without interpolating data on a regular range.

TABLE 2 – Distribution values from CDF and analysis program at centreline

	PDF	Analysis Program	Unit	Relative error
$\overline{u}$	5.24	5.23	m/s	0.08 %
u_{rms}	2.01×10^{-1}	2.01×10^{-1}	m/s	0.06 %
S_u	-5.50×10^{-1}	-4.75×10^{-1}	-	15.7 %

5.4   Comments on spectra

The matching of curves from different locations at figure 7.b seems to agree with Kolmogorov's predictions on universal laws of turbulence at small scales. The three one dimensional spectra fits very properly the one with the other after being made dimensionless using $\kappa^* = \kappa\eta$ and F_{11}^* from F_{11} using viscosity and dissipation rate. Concerning three dimensional spectra E made dimensionless at figure 8, the many operations to obtain it may have altered a bit the signal. Nevertheless, there is a range for $\kappa \gtrsim 7e-2$ where the three spectra match pretty well. That being said, the slope in this range seems to be slightly greater (in absolute value) than the $-5/3$ Kolmogorov's prediction.

13

6   Error Analysis

We propose a brief overview of error analysis in this section. For further analysis one can have a look at [Derksen, 1995]. Since our results come from measurements that are processed sometimes quite a lot, it can be interesting to keep in mind the different sources of errors. We can separate them in three groups : the errors that are inherent of the studied phenomena, the ones that comes from the data acquisition and finally the propagation of this error through data processing.

Measurement of statistical values of a flow deals directly with the random characteristic of turbulence. Turbulent fluctuations of velocity and pressure are characterized by the width of the probability density function. The RMS value of velocity is therefore a good clue to represent the level of randomness. But there are other random process than turbulence like noise in the flow (at lower scales than Kolmogorov's micro scale) as well as in resistances and electronic devices (temperature fluctuations described by statistical physics theory). The difficulty that brings this kind of noise is to be found in the width of its spectrum which can make it difficult to delete. Moreover as we look at amplified tiny variations of the hot-wire resistance, one should verify that the ratio of noise versus resistance fluctuations due to turbulent intermittency stays under reasonably low values. We also discussed previously about the fact that hot-wire anemometry requires the assumption of a negligible heat capacity so that the change of wire temperature is faster that the change of ambient turbulent velocity. Finally we have to take into account the duration of measurement which will be critical in the averaging process.

The measurement procedure involves several large scale uncertainties. First the King's Law constants are calibrated with a specific precision and we could characterized the precision of this fitting with the residual error in the optimisation process discussed earlier. Moreover this whole calibration is given for a reference room's temperature that might change during the experiment. Otherwise, not only the measurement itself is crucial but also the position y at which it is carried out reveals an uncertainty that can affect the log-law fitting for instance. This uncertainty depends on the tool used to position it at the desired distance from the wall. As we go to a distance ~ 0.13 mm, we may think that the uncertainty is around ~ 0.01 mm. But the experimenter attention is the most critical part here. Finally the conversion from an analog signal to a discretized, sampled and rounded digital one results in a loss of information.

To obtain values of interest from the raw measurements, we carried out lots of mathematical operations : multiplication, power, integral, averaging... that have a direct effect on the uncertainty propagation. There are general conventions to compute the propagation for each operations, as using chain rule derivation for instance. These methods can be found easily in literature.

7 Conclusions

Although we were not able to carry out this laboratory session due to the unfortunate circumstances, the analysis part of this report dealt with the empirical verification of several theoretical predictions on turbulent boundary layers and universal turbulent behaviours and gave an insight on the work required to understand, model and predict turbulent phenomena.

If some people believed that numerical simulations could be a substitute to empirical developpemnts, it has since been demonstrated that this is far from being a reality. In fact, experimental data even regain popularity as today's research in mechanics see new methods taking advantage of great amounts of data and capable of builiding reduced models. An introduction of turbulence and big data can be found at [Pollard et al.,] and an example of a new method (that appeared barely 1-2 years ago) called physics informed neural networks (PINN) applied to PDF modelling [Raissi et al., 2019] and turbulent Couette flow [Mehta et al., 2019] could bring promising outlooks.

The entire code will be available on the Github :

<div align="center">github.com/GRaynaud/MECH656_Lab_Gaetan_Raynaud</div>

You will find `Python`'s script in the `Python` folder. Especially you might be interested in the following files :

1. `CalibrationAnemometer.py` that computes and displays King's Law constant
2. `PDF_function.py` that defines the custom PDF function and uses it for the required computations
3. `U_Momentum_Analysis.py` that outputs all the required profiles and fits the log-law
4. `Spectrum.py` Compute the 3D spectra in a dimensionless form

Références

[Derksen, 1995] Derksen, R. W. (1995). Calibration error and the measurement of turbulence statistics. *Environmetrics*, 6(6) :651–658.

[Goushcha et al., 2015] Goushcha, O., Akaydin, H., Elvin, N., and Andreopoulos, Y. (2015). Energy harvesting prospects in turbulent boundary layers by using piezoelectric transduction. *Journal of Fluids and Structures*, 54 :823–847.

[Mathis et al., 2011] Mathis, R., Marusic, I., Hutchins, N., and Sreenivasan, K. R. (2011). The relationship between the velocity skewness and the amplitude modulation of the small scale by the large scale in turbulent boundary layers. *Physics of Fluids*, 23(12) :121702.

[Mehta et al., 2019] Mehta, P. P., Pang, G., Song, F., and Karniadakis, G. E. (2019). Discovering a universal variable-order fractional model for turbulent Couette flow using a physics-informed neural network. *Fractional Calculus and Applied Analysis*, 22(6) :1675–1688.

[Pollard et al.,] Pollard, A., Castillo, L., Danaila, L., and Glauser, M. Whither Turbulence and Big Data in the 21st Century ?

[Pope and Pope, 2000] Pope, S. B. and Pope, S. B. (2000). *Turbulent Flows*. Cambridge University Press.

[Raissi et al., 2019] Raissi, M., Babaee, H., and Givi, P. (2019). Deep learning of turbulent scalar mixing. *Phys. Rev. Fluids*, 4(12) :124501.

[Strahle and Neale, 1981] Strahle, W. C. and Neale, D. H. (1981). Turbulence-Generated Pressure Fluctuations in a Rocket-Like Cavity. *AIAA Journal*, 19(3) :360–365.

[Tennekes et al., 1972] Tennekes, E. P. o. A. E. H., Tennekes, H., Lumley, J. L., Lumley, J. L., and Technology, M. I. o. (1972). *A First Course in Turbulence*. MIT Press.

[Weaver et al., 2000] Weaver, D. S., Ziada, S., Au-Yang, M. K., Chen, S. S., Paı¨doussis, M. P., and Pettigrew, M. J. (2000). Flow-Induced Vibrations in Power and Process Plant Components—Progress and Prospects. *Journal of Pressure Vessel Technology*, 122(3) :339–348.